LETTER

Extreme hydrothermal conditions at an active plate–bounding fault

Rupert Sutherland[1,2], John Townend[2], Virginia Toy[3], Phaedra Upton[1], Jamie Coussens[4], Michael Allen[5], Laura-May Baratin[2], Nicolas Barth[6], Leeza Becroft[3], Carolin Boese[2], Austin Boles[7], Carolyn Boulton[5], Neil G. R. Broderick[8], Lucie Janku-Capova[2], Brett M. Carpenter[9], Bernard Célérier[10], Calum Chamberlain[2], Alan Cooper[3], Ashley Coutts[8], Simon Cox[11], Lisa Craw[3], Mai-Linh Doan[12], Jennifer Eccles[8], Dan Faulkner[5], Jason Grieve[3], Julia Grochowski[2], Anton Gulley[8], Arthur Hartog[13], Jamie Howarth[1], Katrina Jacobs[2], Tamara Jeppson[14], Naoki Kato[15], Steven Keys[2], Martina Kirilova[3], Yusuke Kometani[16], Rob Langridge[1], Weiren Lin[17,18], Timothy Little[2], Adrienn Lukacs[3], Deirdre Mallyon[19], Elisabetta Mariani[5], Cécile Massiot[1,2], Loren Mathewson[3], Ben Melosh[20], Catriona Menzies[4], Jo Moore[21], Luiz Morales[22], Chance Morgan[9], Hiroshi Mori[23], Andre Niemeijer[24], Osamu Nishikawa[25], David Prior[3], Katrina Sauer[3], Martha Savage[2], Anja Schleicher[7,26], Douglas R. Schmitt[19], Norio Shigematsu[27], Sam Taylor-Offord[2], Damon Teagle[4], Harold Tobin[14], Robert Valdez[28], Konrad Weaver[2], Thomas Wiersberg[26], Jack Williams[3], Nick Woodman[4] & Martin Zimmer[26]

Temperature and fluid pressure conditions control rock deformation and mineralization on geological faults, and hence the distribution of earthquakes[1]. Typical intraplate continental crust has hydrostatic fluid pressure and a near-surface thermal gradient of 31 ± 15 degrees Celsius per kilometre[2,3]. At temperatures above 300–450 degrees Celsius, usually found at depths greater than 10–15 kilometres, the intra-crystalline plasticity of quartz and feldspar relieves stress by aseismic creep and earthquakes are infrequent. Hydrothermal conditions control the stability of mineral phases and hence frictional–mechanical processes associated with earthquake rupture cycles, but there are few temperature and fluid pressure data from active plate-bounding faults. Here we report results from a borehole drilled into the upper part of the Alpine Fault, which is late in its cycle of stress accumulation and expected to rupture in a magnitude 8 earthquake in the coming decades[4,5]. The borehole (depth 893 metres) revealed a pore fluid pressure gradient exceeding 9 ± 1 per cent above hydrostatic levels and an average geothermal gradient of 125 ± 55 degrees Celsius per kilometre within the hanging wall of the fault. These extreme hydrothermal conditions result from rapid fault movement, which transports rock and heat from depth, and topographically driven fluid movement that concentrates heat into valleys. Shear heating may occur within the fault but is not required to explain our observations. Our data and models show that highly anomalous fluid pressure and temperature gradients in the upper part of the seismogenic zone can be created by positive feedbacks between processes of fault slip, rock fracturing and alteration, and landscape development at plate-bounding faults.

Borehole measurements from intraplate regions reveal near-hydrostatic fluid pressures and linear increases in effective stress with depth that are consistent with the crust being close to brittle failure and containing faults with friction coefficients of 0.6–1.0 and low cohesive strengths[3]. Laboratory measurements for many natural rocks have a similar (Byerlee) range of frictional strengths[6]. However, major active faults at plate boundaries appear anomalously weak. For example, the maximum horizontal stress adjacent to the San Andreas Fault in California is oriented at a high angle (65°–85°) to the fault and, despite ambient stress magnitudes similar to those in intra-plate regions, the geometry of the stress field yields a low shear stress resolved onto the fault, and hence a lower inferred frictional strength than that predicted by Byerlee friction[7]. There is mounting evidence that this is true for many faults[8].

The lack of noticeable heat flow anomalies adjacent to large plate boundary faults, most famously the San Andreas Fault[9], also demonstrates that less work is done on faults than predicted if Byerlee frictional failure dissipated energy as heat. Drilling has revealed that heat generated by >50 m of slip during the Tohoku-Oki 2011 earthquake (moment magnitude $M_w = 9.0$) produced only a small temperature anomaly, requiring an average friction coefficient during slip of <0.1 (ref. 10); similar results were found after the Wenchuan 2008 and Chi-Chi 1999 earthquakes[11,12]. Plate boundary faults must, therefore, be composed of materials that are mechanically weak on long time-scales, even if weakness is a transient phenomenon during movement.

Brittle fault rocks form within the seismogenic zone via the physical comminution of rock and via temperature-sensitive chemical reactions with pore fluids. Experimental studies of dynamic friction confirm that slip weakening by up to one order of magnitude is common as the slip rate approaches values inferred for large earthquakes, though the mechanisms of weakening are debated[13,14]. The evolution of the coefficient of friction on a fault surface during and after an earthquake is time-dependent[15]. Of particular importance is the stability of phyllosilicate phases with low dynamic friction[16], thermal expansion and the generation of physicochemical reaction products produced during slip[13], and the presence of low-permeability mineral cements

[1]GNS Science, PO Box 30368, Lower Hutt, New Zealand. [2]SGEES, Victoria University of Wellington, PO Box 600, Wellington, New Zealand. [3]Department of Geology, University of Otago, PO Box 56, Dunedin 9054, New Zealand. [4]Department of Ocean and Earth Science, University of Southampton, Southampton SO14 3ZH, UK. [5]School of Environmental Sciences, University of Liverpool, Liverpool L69 3GP, UK. [6]Department of Earth Sciences, University of California, Riverside, California 92521, USA. [7]Department of Earth and Environmental Sciences, University of Michigan, Ann Arbor, Michigan 48109, USA. [8]University of Auckland, Private Bag 92019, Auckland 1142, New Zealand. [9]School of Geology and Geophysics, University of Oklahoma, Norman, Oklahoma 73019, USA. [10]CNRS, Université de Montpellier, 34095 Montpellier, France. [11]GNS Science, Private Bag 1930, Dunedin 9054, New Zealand. [12]Université Grenoble-Alpes, Université Savoie Mont Blanc, CNRS, IRD, IFSTTAR, ISTerre, F-38000 Grenoble, France. [13]Schlumberger Fiber-Optic Technology Centre, Romsey, Hampshire SO51 9DL, UK. [14]Department of Geoscience, University of Wisconsin-Madison, Madison, Wisconsin 53706, USA. [15]Department of Earth and Space Science, Osaka University, Osaka 565-0871, Japan. [16]Department of Geosphere Sciences, Yamaguchi University, Yamaguchi 753-8511, Japan. [17]Graduate School of Engineering, Kyoto University, Kyoto 615-8540, Japan. [18]Kochi Institute for Core Sample Research, Japan Agency for Marine-Earth Science and Technology, Kochi 783-8502, Japan. [19]Department of Physics, University of Alberta, Edmonton, Alberta T6G 2R3, Canada. [20]Department of Earth and Planetary Sciences, McGill University, Montreal, Quebec H3A 0G4, Canada. [21]Department of Earth and Planetary Sciences, Macquarie University, Sydney, New South Wales 2109, Australia. [22]ScopeM, ETH, 8093 Zürich, Switzerland. [23]Department of Geology, Shinshu University, Matsumoto, Asahi 3-1-1, Japan. [24]Faculty of Geosciences, HPT Laboratory, Utrecht University, 3584 CD Utrecht, The Netherlands. [25]Department of Earth Science and Technology, Akita University, Akita City 010-8502, Japan. [26]GFZ German Research Centre for Geosciences, Telegrafenberg, 14473 Potsdam, Germany. [27]Geological Survey of Japan, AIST, Tsukuba, Japan. [28]Department of Geosciences, Pennsylvania State University, University Park, Pennsylvania 16802, USA.
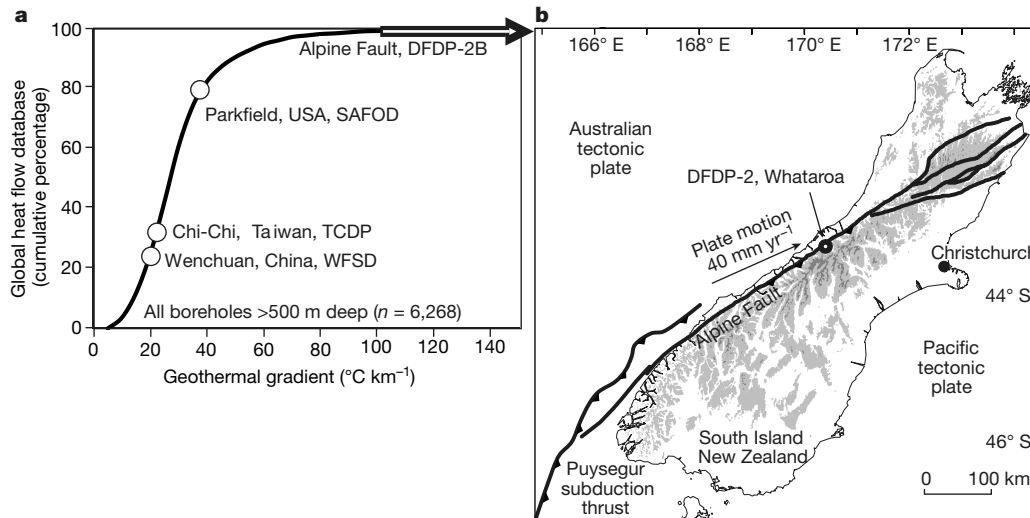
Figure 1 | Global context and regional setting. a, Geothermal gradient measured in DFDP-2B compared to global continental measurements (black curve) and previous active fault drilling measurements (circles) (Data are taken from the Global Heat Flow Database of the International Heat Flow Commission, version 2010, http://www.heatflow.und.edu.) SAFOD, the San Andreas Fault Observatory at Depth, USA; TCDP, the Taiwan Chelungpu-Fault Drilling Project; WFSD, the Wenchuan Earthquake Fault Scientific Drilling, China. **b**, Location on the Australia–Pacific tectonic plate boundary of borehole DFDP-2B at 43.29065° S (WGS84 datum), 170.40646° E, with local depth datum at 94.84 m (NZGD2009 datum).

that enhance dynamic fluid pressurization mechanisms[17]. Temperature and fluids within fault zones are primary controls on material properties and slip-weakening mechanisms, and hence they strongly influence earthquake processes.

Scientific drilling is the only way to determine ambient conditions directly and to measure physical and chemical properties within active fault zones[8]. Drilling studies have taken place in response to earthquakes of $M_w = 6.9$–9.0 in Japan, Taiwan, China and the USA[8,10–12,18–21], and the results do not reveal anomalous temperatures or fluid pressures (Fig. 1). Borehole injection experiments, earthquake aftershock studies, and laboratory experiments on fault zone materials reveal that the

earthquake process perturbs the fault zone, which then heals during the post-seismic period[22–26].

The Alpine Fault of southern New Zealand is a major plate boundary fault (Fig. 1) that produces large earthquakes every 291 ± 23 years and last ruptured in AD 1717[4,5]. It has a Quaternary oblique dextral-reverse slip rate[27] of 26 ± 5 mm yr^{-1}. The oblique dextral-reverse slip has exhumed a suite of fault rocks from depths of 30 km in the past few million years[27]. The primary motivation of the Deep Fault Drilling Project (DFDP) is to understand ambient conditions, rock properties and geophysical phenomena immediately before a large earthquake, because little is known about active geological faults before they slip,
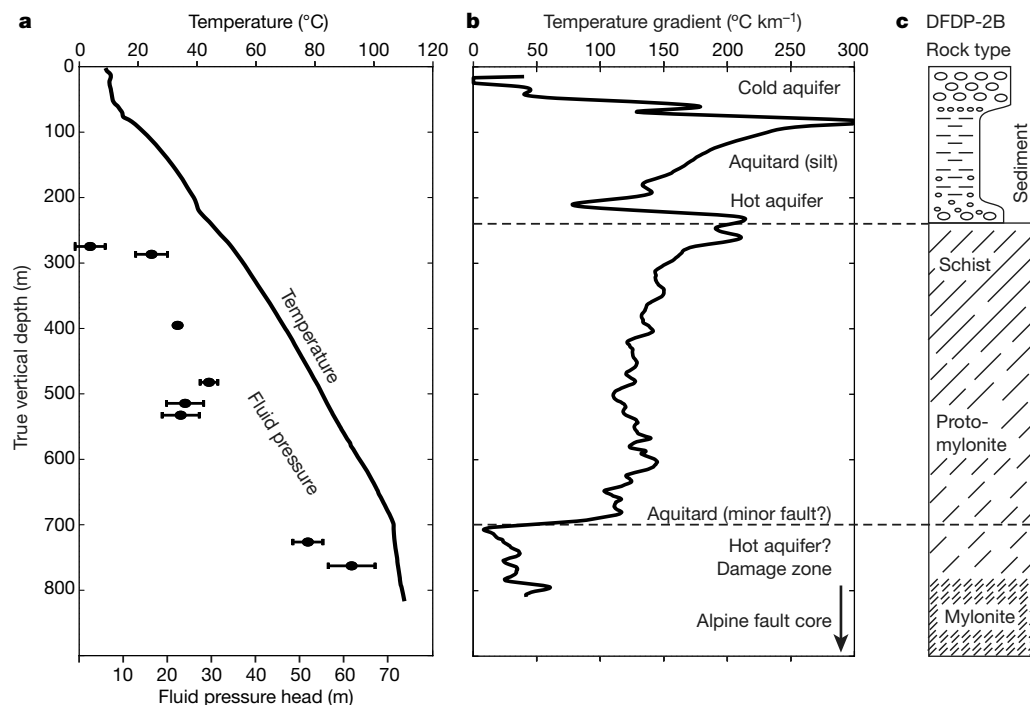

Figure 2 | DFDP-2B borehole results. a, Observed mean temperature 7–14 months after drilling (solid line; see Source Data for this figure online); and equilibrated fluid pressure estimates (circles, error bars show two standard errors) determined from mud pressure equilibration experiments carried out during breaks in drilling (Extended Data Tables 1 and 2). **b**, Temperature gradient and inferred locations of aquifers and aquitards. **c**, Geological summary. Source Data for Fig. 2 is available online.
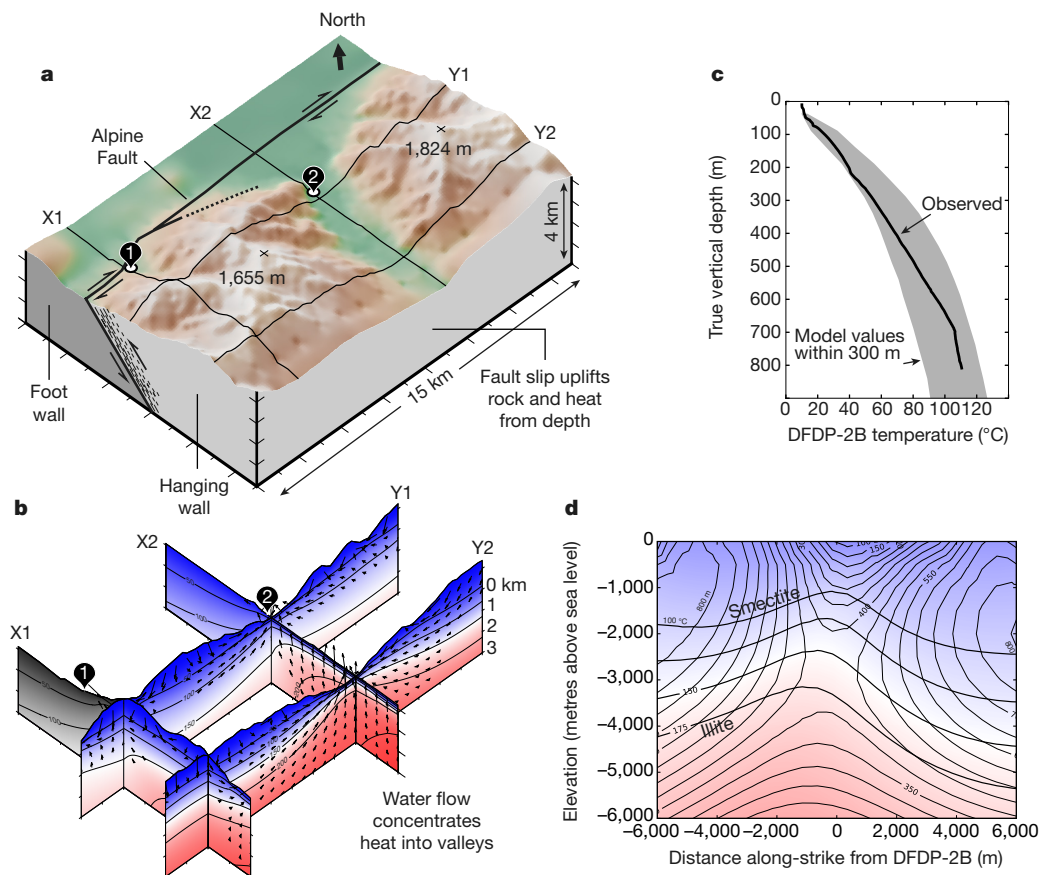
Figure 3 | Thermal and fluid flow models. a, DFDP-1 and DFDP-2 locations (marked 1 and 2, respectively), the Alpine Fault and topography. The hanging wall is Mesozoic amphibolite facies meta-greywacke, with a transition through protomylonite to mylonite to cataclasite in proximity to the principal slip zone[27]. The foot wall is composed of Palaeozoic granitoids that intrude quartzose metasediments. **b**, Temperature cross-sections with contours (in degrees Celsius) and fluid fluxes (arrows show fluxes >0.15 m yr^{-1}) extracted from a three-dimensional numerical model with 200 m horizontal resolution near DFDP-2 (Extended Data Fig. 4).

Parameters for the model shown are: (1) a dip-slip rate of 8 mm yr^{-1}; and (2) uniform permeability of 5.0×10^{-16} m^2 in a layer above 5 km below sea level within the Alpine Fault hanging wall. **c**, Comparison of model values (as shown in **b**), extracted from within 300 m of DFDP-2B (grey shading), with borehole observations. **d**, Fluid pressure and temperature inferred on the Alpine Fault plane. Thin lines are fluid pressure head (in metres, with reference to the density of water at the surface); and bold lines are temperature contours approximately equivalent to the temperature of illite–smectite transitions (100–175 °C).

and initial conditions are assumed to affect earthquake nucleation, rupture and seismic radiation.

Drilling of the DFDP-2B borehole was completed on 8 December 2014. We penetrated a sequence of Quaternary gravel and lake silt, schist, protomylonite and mylonite (Fig. 2). The base of the borehole is estimated to be within 200–400 m of the principal slip-zone gouge, on the basis of site surveys and measurement of quartz grain sizes and textures in drill cuttings that are similar to mylonitic fault rocks exposed nearby. Comprehensive rock, mud, wireline (that is, down-hole geophysical), and seismological observations were collected, and a fibre-optic cable was installed after drilling to acquire repeated precise temperature measurements.

Post-drilling equilibrated temperatures in the borehole reveal a zone above 700 m of true vertical depth (740 m drilled depth) characterized by a gradient of 100–200 °C km^{-1}, and a deeper zone with a gradient of 30–50 °C km^{-1} (Fig. 2). The fluid pressure gradient in the borehole below the sedimentary layers is 8%–10% above hydrostatic, but an aquifer at the base of the sediments (230–240 m) is only slightly over-pressured (<5 m head), meaning that the silts do not constitute a total hydraulic seal (Fig. 2).

The geothermal gradient in the upper 700 m of the DFDP-2B borehole is unusual by global standards: 99% of geothermal gradients measured in deep (>500 m) boreholes elsewhere are less than 80 °C km^{-1} (ref. 2; Fig. 1). Values exceeding 80 °C km^{-1} are typically associated with volcanic regions, but there is no evidence for Neogene

volcanism near the DFDP-2B site. The regional value determined from petroleum boreholes west of DFDP-2B is about 30 °C km^{-1} (ref. 28).

We model the thermal state near DFDP sites by considering simultaneous heat transport via (1) conduction, (2) rock advection driven by fault slip, and (3) fluid advection driven by local topography (Fig. 3). We assume uniform high permeability to some fixed depth (3 km or 5 km) above the principal slip zone of the Alpine Fault and low permeability beneath it. Adjustable parameters are the value of high permeability, and the rate of reverse dip-slip fault movement, which is constrained by geological observations of late Quaternary offsets to lie within the range 6–14 mm yr^{-1} near the drilling site[27]. Drilling-related temperature anomalies are modelled separately and excluded from our analysis by selecting observations made more than six months after drilling (Extended Data Figs 1 and 2). There is little variability in thermal diffusivity within the borehole (Extended Data Fig. 3). The three-dimensional model domain (Extended Data Fig. 4) is much larger than the specific region of interest. See Methods for details.

We aim to fit temperature observations from DFDP-2B (Fig. 2) and the geothermal gradient of 62 ± 2 °C km^{-1} measured in the 150-m-deep DFDP-1B borehole (Fig. 3)[29]. Our models are intentionally simplified, because they are under-constrained by observations, and intended only to gain general insight into hydrothermal structure in and around the fault zone. The best fit to DFDP-2B temperature observations is obtained with a fault dip-slip rate of 14 mm yr^{-1} and low permeability, but this solution does not fit DFDP-1B observations (Extended Data

Fig. 5). The relatively low average curvature of the thermal profile, combined with the over-simplified hydrological structure, leads to an inference that rock advection and thermal diffusion are the primary heat transport mechanisms at 240–740 m depth in DFDP-2B; but the large difference in geothermal gradient between DFDP-1B and DFDP-2B requires that fluid advection is important in heat transfer between sites and also requires a regional value of permeability $>5 \times 10^{-16}$ m^2 (Extended Data Fig. 5). The DFDP-2B fluid pressure gradient indicates upward flow through the fractured rock mass near the borehole (Fig. 2a).

The models are broadly consistent with existing knowledge of fault slip rate and heterogeneous rock permeability in the hanging wall of the Alpine Fault. We expect permeability to be low within cataclasites near the principal slip zone and minor fault splays[29], and that these cataclasites and splays will be barriers to fault-normal flow. We expect high permeability within the damage zone, producing an aquifer that enhances fault-parallel flow, and beneath mountains of the hanging wall where warm springs are common[30]. The region of relatively low geothermal gradient at the base of DFDP-2B (Fig. 2) is a discrete hydrological domain and interpreted as an aquifer associated with the damage zone, but we were unable to verify its properties owing to engineering difficulties. Fluid pressure equilibration experiments ('slug tests') conducted during drilling of DFDP-2B indicate bulk-rock permeability around the borehole of the order of 10^{-15} m^2 (Extended Data Tables 1 and 2). In summary, we infer that fault slip moves rock and heat from depth, and topographically driven fluid flow through fractured rocks concentrates heat into valleys (Fig. 3).

Our results have broad implications for understanding earthquakes and fault zone geology, because temperature and fluid pressure anomalies inferred close to the principal slip zone are large. Lateral changes in temperature and fluid pressure may exceed 50 °C and 4 MPa, respectively (Fig. 3d), and this must affect chemical, mineralogical and seismogenic processes. Our models predict considerable along-strike variations in the depth of smectite alteration (<100–175 °C), which may influence dynamic fault strength at shallow depths during earthquakes. In some hanging-wall valley locations, our models predict that pore fluid temperatures could exceed 200 °C at only 1 km depth, and nearby future boreholes could sample the Alpine Fault principal slip zone at temperatures above the smectite–illite transition. Large along-strike temperature anomalies cause pore fluid density and viscosity variations that influence fluid–rock interactions and provide a mechanism for deeper fluid convection, even though heat transport by fluids in low-permeability deeper rocks may be minor. Mineralogical evidence from near the Alpine Fault confirms that boiling occurs in the upper and mid-crust[31] and that meteoric fluids circulate through the entire seismogenic zone[32].

Online Content Methods, along with any additional Extended Data display items and Source Data, are available in the online version of the paper; references unique to these sections appear only in the online paper.

1. Sibson, R. H. Fault zone models, heat flow, and the depth distribution of earthquakes in the continental crust of the United States. *Bull. Seismol. Soc. Am.* **72,** 151–163 (1982).
2. Pollack, H. N., Hurter, S. J. & Johnson, J. R. Heat flow from the Earth's interior: analysis of the global data set. *Rev. Geophys.* **31,** 267–280 (1993).
3. Townend, J. & Zoback, M. D. How faulting keeps the crust strong. *Geology* **28,** 399–402 (2000).
4. Cochran, U. *et al.* A plate boundary earthquake record from a wetland adjacent to the Alpine fault in New Zealand refines hazard estimates. *Earth Planet. Sci. Lett.* **464,** 175–188 (2017).
5. Sutherland, R. *et al.* in *A Continental Plate Boundary: Tectonics at South Island, New Zealand Geophysical Monograph Series* (eds Okaya, D., Stern, T. A. & Davey, F.) 235–251 (American Geophysical Union, 2007).
6. Byerlee, J. Friction of rocks. *Pure Appl. Geophys.* **116,** 615–626 (1978).
7. Townend, J. & Zoback, M. D. Regional tectonic stress near the San Andreas fault in central and southern California. *Geophys. Res. Lett.* **31,** L15S11 (2004).
8. Zoback, M. D., Hickman, S. & Ellsworth, W. in *Treatise on Geophysics* (ed. Schubert, G.) 649–674 (Elsevier, 2007).
9. Fulton, P. M., Saffer, D. M., Harris, R. N. & Bekins, B. A. Re-evaluation of heat flow data near Parkfield, CA: evidence for a weak San Andreas Fault. *Geophys. Res. Lett.* **31,** L15S15 (2004).
10. Fulton, P. *et al.* Low coseismic friction on the Tohoku-Oki fault determined from temperature measurements. *Science* **342,** 1214–1217 (2013).
11. Kano, Y. *et al.* Heat signature on the Chelungpu fault associated with the 1999 Chi-Chi, Taiwan earthquake. *Geophys. Res. Lett.* **33,** L14306 (2006).
12. Li, H. *et al.* Long-term temperature records following the Mw 7.9 Wenchuan (China) earthquake are consistent with low friction. *Geology* **43,** 163–166 (2015).
13. Di Toro, G. *et al.* Fault lubrication during earthquakes. *Nature* **471,** 494–498 (2011).
14. Kanamori, H. & Brodsky, E. E. The physics of earthquakes. *Rep. Prog. Phys.* **67,** 1429–1496 (2004).
15. Dieterich, J. H. Modeling of rock friction: 1. Experimental results and constitutive equations. *J. Geophys. Res. Solid Earth* **84,** 2161–2168 (1979).
16. Carpenter, B., Marone, C. & Saffer, D. Weakness of the San Andreas Fault revealed by samples from the active fault zone. *Nat. Geosci.* **4,** 251–254 (2011).
17. Wibberley, C. A. & Shimamoto, T. Earthquake slip weakening and asperities explained by thermal pressurization. *Nature* **436,** 689–692 (2005).
18. Ohtani, T. *et al.* Fault rocks and past to recent fluid characteristics from the borehole survey of the Nojima fault ruptured in the 1995 Kobe earthquake, southwest Japan. *J. Geophys. Res. Solid Earth* **105,** 16161–16171 (2000).
19. Ma, K. F. *et al.* Slip zone and energetics of a large earthquake from the Taiwan Chelungpu-fault Drilling Project. *Nature* **444,** 473–476 (2006).
20. Williams, C. F., Grubb, F. V. & Galanis, S. P. Heat flow in the SAFOD pilot hole and implications for the strength of the San Andreas Fault. *Geophys. Res. Lett.* **31,** L15S14 (2004).
21. Chester, F. M. *et al.* Structure and composition of the plate-boundary slip zone for the 2011 Tohoku-Oki earthquake. *Science* **342,** 1208–1211 (2013).
22. Kitagawa, Y., Fujimori, K. & Koizumi, N. Temporal change in permeability of the Nojima fault zone by repeated water injection experiments. *Tectonophysics* **443,** 183–192 (2007).
23. Morrow, C. A., Moore, D. E. & Lockner, D. A. Permeability reduction in granite under hydrothermal conditions. *J. Geophys. Res. Solid Earth* **106,** 30551–30560 (2001).
24. Brenguier, F. *et al.* Postseismic relaxation along the San Andreas fault at Parkfield from continuous seismological observations. *Science* **321,** 1478–1481 (2008).
25. Schaff, D. P. & Beroza, G. C. Coseismic and postseismic velocity changes measured by repeating earthquakes. *J. Geophys. Res. Solid Earth* **109,** B10302 (2004).
26. Xue, L. *et al.* Continuous permeability measurements record healing inside the Wenchuan earthquake fault zone. *Science* **340,** 1555–1559 (2013).
27. Norris, R. J. & Cooper, A. F. in *A Continental Plate Boundary: Tectonics at South Island, New Zealand Geophysical Monograph Series* (eds Okaya, D., Stern, T. A. & Davey, F.) 157–175 (American Geophysical Union, 2007).
28. Townend, J. Heat flow through the West Coast, South Island, New Zealand. *N. Z. J. Geol. Geophys.* **42,** 21–31 (1999).
29. Sutherland, R. *et al.* Drilling reveals fluid control on architecture and rupture of the Alpine fault, New Zealand. *Geology* **40,** 1143–1146 (2012).
30. Cox, S. *et al.* Changes in hot spring temperature and hydrogeology of the Alpine Fault hanging wall, New Zealand, induced by distal South Island earthquakes. *Geofluids* **15,** 216–239 (2015).
31. Craw, D. Shallow-level metamorphic fluids in a high uplift rate metamorphic belt; Alpine schist, New Zealand. *J. Metamorph. Geol.* **6,** 1–16 (1988).
32. Upton, P., Koons, P. O. & Chamberlain, C. P. Penetration of deformation-driven meteoric water into ductile rocks; isotopic and model observations from the Southern Alps, New Zealand. *N. Z. J. Geol. Geophys.* **38,** 535–543 (1995).

Author Contributions The drilling experiment and this paper were led by R.S., J.T. and V.T. Thermal and hydraulic modelling and pre-drill planning were done by P.U., J.C., N.W., D.T., C.M. and A.H. All authors except N.G.R.B., N.W. and D.T. contributed to science goals on-site during drilling. Post-drill optical fibre temperature measurements and analysis were performed by R.S., N.G.R.B., L.J.-C., C.C., L.-M.B. and A.H.

METHODS

Temperature observations were made using wireline logging tools before borehole completion, and an optic-fibre cable after completion. The optic-fibre cable was installed and cemented outside steel casing, and interrogated by distributed temperature sensing (DTS) analysis based on Raman scattering of laser light from a source at the surface[33]. A summary of temperature measurements is shown in Extended Data Fig. 1.

Details of drilling operations, scientific equipment and protocols are published elsewhere[34] and the borehole geometry is provided in the Source Data for Fig. 2. Drilling ended on 8 December 2014 and the steel casing was cemented on 17 December 2014. Residual cement was drilled out from within the casing to a depth of 400 m depth on 8 January 2015 (<4 h operations).

Temperatures measured by logging tools were influenced by the history of drilling fluid circulation in the borehole, but this drilling-related temperature anomaly diffused away and was small (about 1 °C) by January 2015. There is a high level of repeatability between later measurements (Extended Data Fig. 2), and the very small temperature variation of about 0.3 °C observed between March 2015 and February 2016 is not converging exponentially on a single value with time. We interpret these changes to represent a non-drilling-related phenomenon. The Source Data for Fig. 2 contains an average value of the four latest profiles, which were measured between July 2015 and February 2016 and are not affected by borehole operations. Observed thermal equilibration times of several weeks are consistent with the bulk thermal diffusivity profile in the borehole that was inferred from mineralogical analysis of rock cuttings (Extended Data Fig. 3).

Pore fluid pressure values (Fig. 1) were derived from analyses of mud level equilibration during breaks in drilling. Equilibrium borehole hydraulic heads were estimated at a range of borehole lengths (Extended Data Tables 1 and 2). These observations were modelled with an exponential function ($R^2 > 0.93$ for all tests) by adjusting three parameters: the initial mud level perturbation, the decay constant and the equilibrium mud level, M. Hydraulic head, H, was then calculated using the measured mud density, D, and the vertical length of the borehole at the time of the test, L, using the equation $H = D(L + M) - L$.

Thermal and hydrological models were constructed and solved using FLAC3D (version 5.0, finite difference method, Itasca Consulting Group, http://www.itascacg.com/software/flac3d) and FEFLOW (finite element method, MIKE Powered by DHI, https://www.mikepoweredbydhi.com/products/feflow). The numerical solution was computed in two steps. In the first step, a two-dimensional crustal exhumation model, similar to previous geodynamic models that predict localization of slip on the Alpine Fault[35], was simulated using FLAC3D to a depth of 30 km for 10 million years. The rate of dip-slip movement was treated as a variable parameter. The two-dimensional result was then used to apply a basal temperature boundary condition to a three-dimensional model with topography (Extended Data Fig. 4; FLAC3D and FEFLOW solutions). No-flow boundary conditions were applied for fluid and heat at the sides of the model. At the basal surface, a no-fluid-flow condition was imposed. An atmospheric temperature and pore pressure condition was applied at the top surface. A low permeability of 10^{-18} m² was imposed beneath the fault. The heat equation solved is:

$$\partial T / \partial t = H/C_b + \kappa_b \nabla \cdot \nabla T - (C_f/C_b)\boldsymbol{u}_f \cdot \nabla T - (C_r/C_b)\boldsymbol{u}_r \cdot \nabla T = 0$$

where H is internal heat productivity, κ_b is the bulk thermal diffusivity, T is temperature, C_f, C_r and C_b are volumetric heat capacities of fluid, rock and the bulk mixture, respectively, $\boldsymbol{u}_f$ and $\boldsymbol{u}_r$ are the vector fluxes of fluid and rock respectively, and $\nabla = (\partial/\partial x, \partial/\partial y, \partial/\partial z)$ is the gradient operator.

Uniform permeability above the fault was treated as a variable parameter. In initial simulations using FLAC3D the permeability extended to 5 km below sea level. A hanging-wall permeability of $(5.5 \pm 2.0) \times 10^{-16}$ m² and a fault dip-slip rate of 7.7 ± 2.7 mm yr^{-1} produced an adequate fit to DFDP-2 observations, but with a strong trade-off between the two parameters: faster dip-slip rates require lower permeabilities. Model runs were then completed using FEFLOW with uniform permeability to 3 km below sea level and temperature-dependent fluid density. Results are shown in Extended Data Figs 5, 6 and 7. Because density was temperature-dependent in FEFLOW model runs, we report hydraulic conductivity (factor of about 10^{-7} conversion at the near surface).

We did not limit fluid recharge rate or allow the piezometric surface to adjust. If we had, then even higher values of permeability could fit our data and may be more realistic: the piezometric surface and lateral fluid pressure gradients would be lowered. It is likely that permeability is both anisotropic and localized, for example, within and near the damage zone, along lithologic layers, or within fractured zones. However, such models are under-constrained by observations, so were not constructed. Minor faults may also create local seals that compartmentalize flow.

Data availability. Data that support the findings of this study are available as Extended Data Tables 1 and 2 and Source Data for Fig. 1. Additional relevant data (for example, individual temperature logs shown in Extended Data Fig. 1) will be made available online[35], in forthcoming publications, or data are available from the corresponding author upon reasonable request.

33. Hartog, A. in *Optical Fiber Sensor Technology* 241–301 (Springer, 2000).
34. Sutherland, R. *et al.* Deep Fault Drilling Project (DFDP), Alpine Fault boreholes DFDP-2A and DFDP-2B technical completion report. *GNS Sci. Rep.* **2015,** 1–269 (2015).
35. Upton, P. & Koons, P. O. in *A Continental Plate Boundary: Tectonics at South Island, New Zealand* Vol. 175 (eds Okaya, D., Stern, T. A. & Davey, F.) 253–270 (American Geophysical Union, 2007).
36. Sutherland, R. *et al.* Deep Fault Drilling Project DFDP-1 and -2. Operational Datasets version 1, http://doi.org/10.5880/ICDP.5052.001 (GFZ Data Services, 2017).
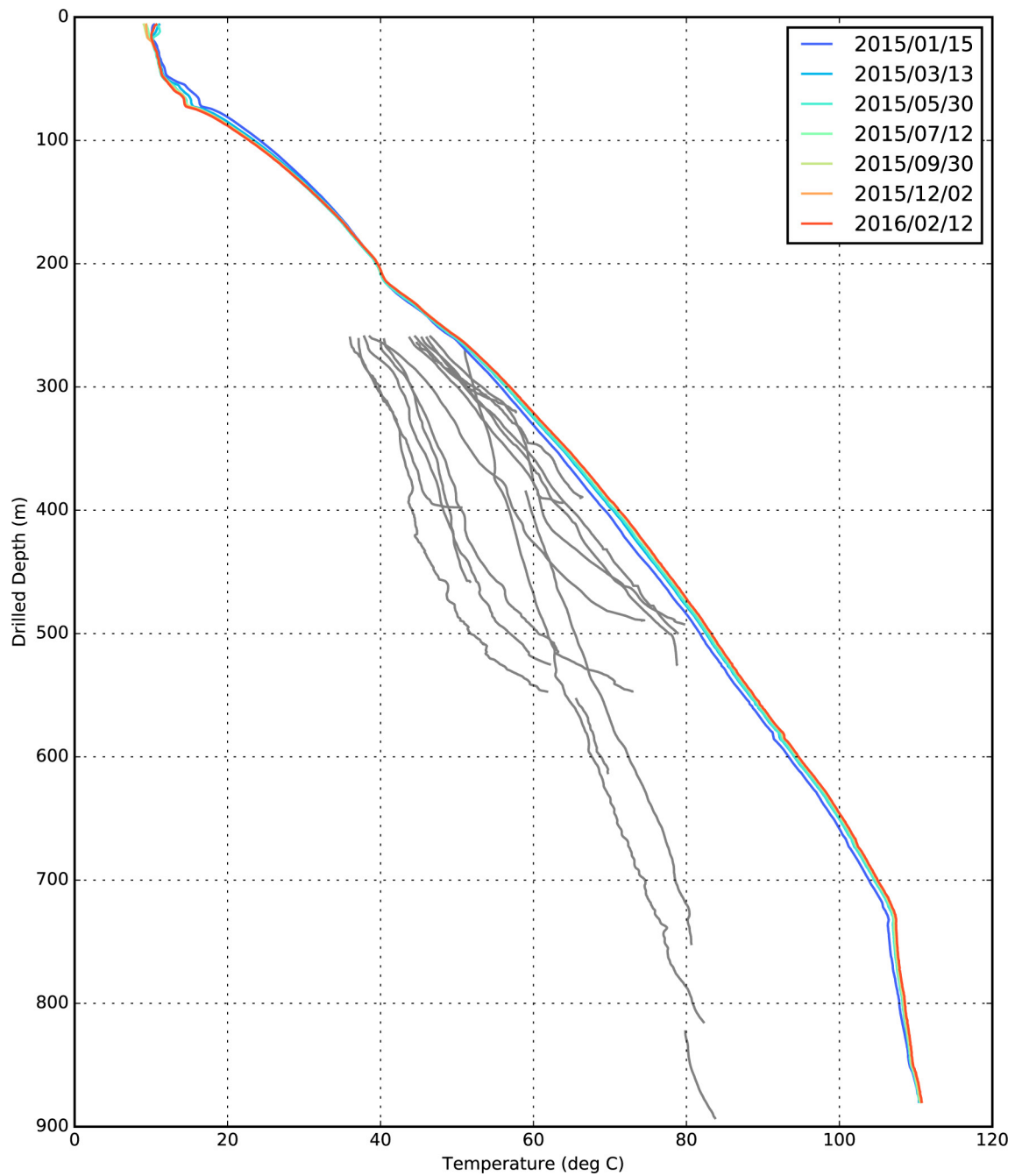
Extended Data Figure 1 | Borehole temperature measurements taken on successive dates (year/month/day). Grey lines indicate measurements using logging tools; coloured lines those taken using DTS.
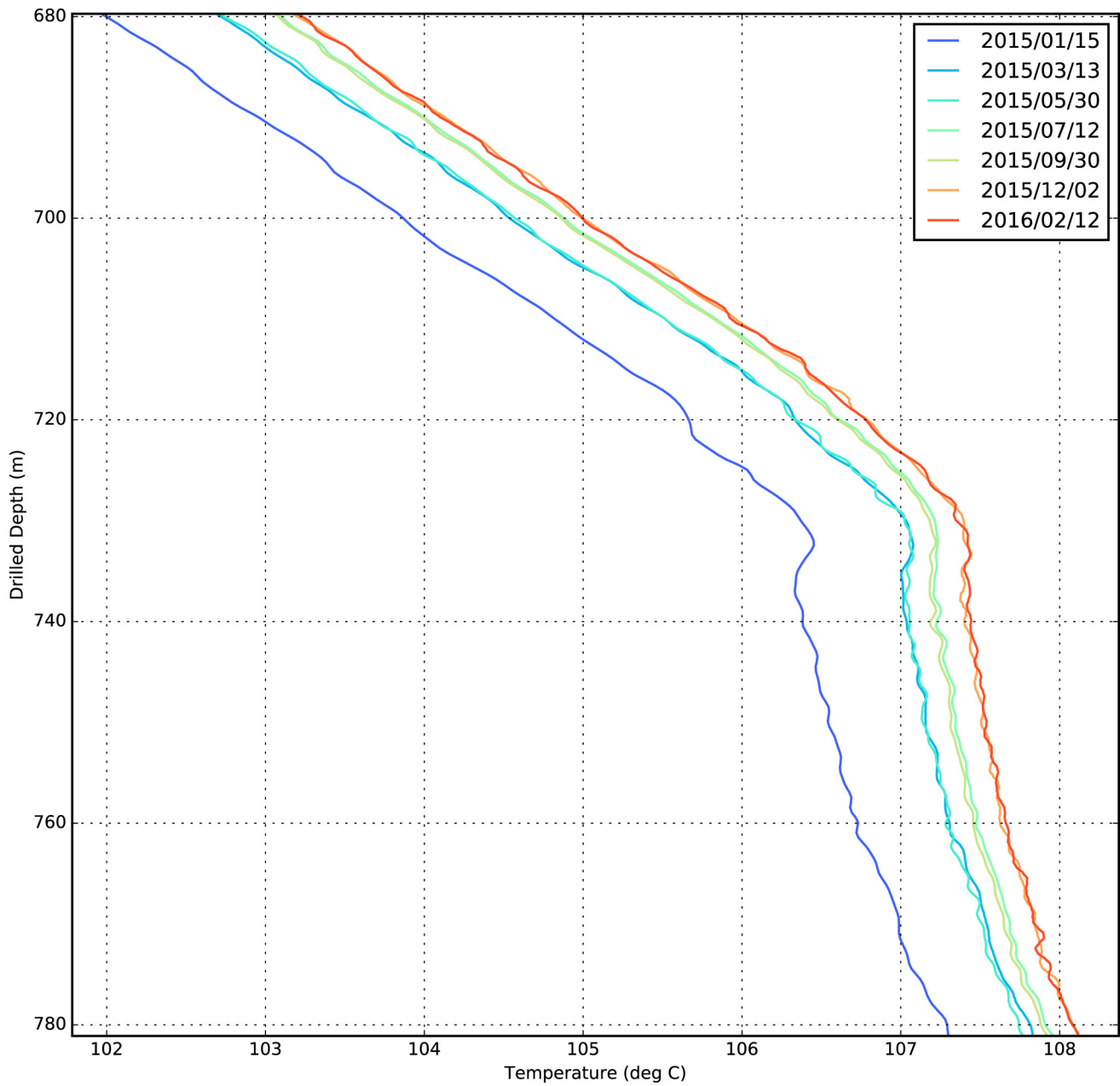
Extended Data Figure 2 | Enlargement of borehole temperature measurements, showing that the magnitude of DTS temperature changes with time.
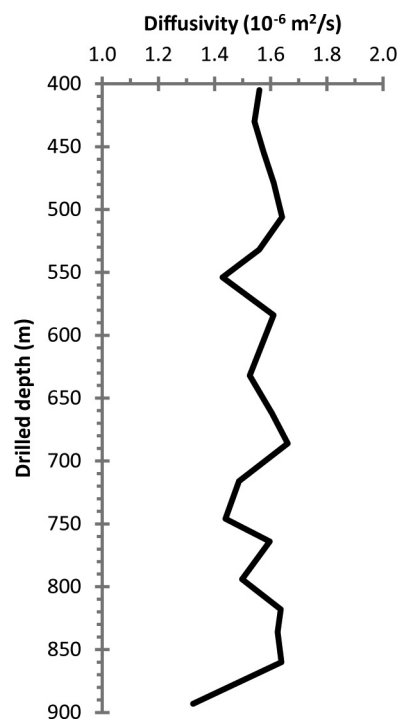
Extended Data Figure 3 | Bulk mean thermal diffusivity profile for borehole DFDP-2B. Data inferred from quantitative X-ray diffraction analysis of rock cuttings (geometric mean of mineral-specific diffusivities).
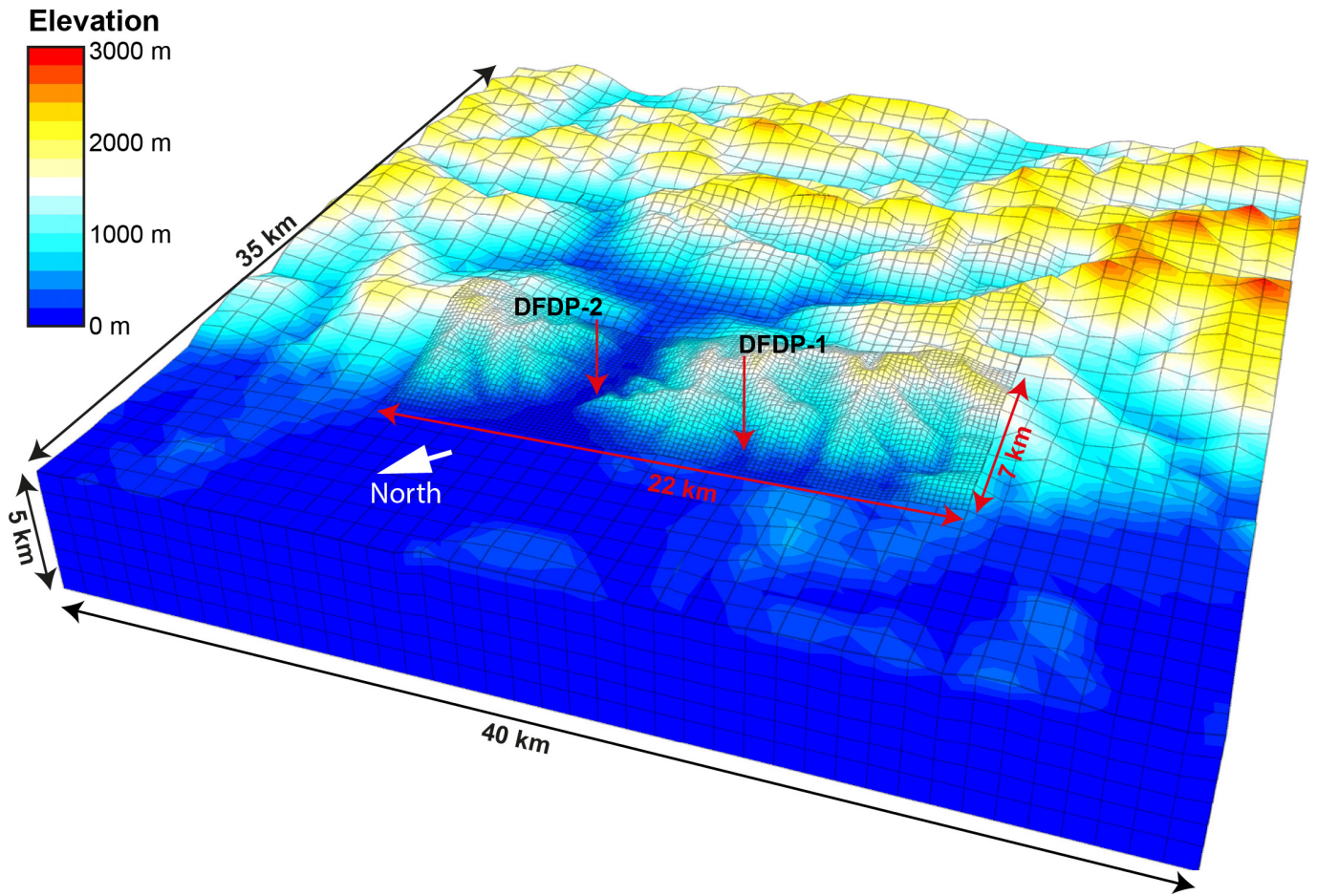
Extended Data Figure 4 | Three-dimensional model mesh geometry with variable node spacing of 200 m, 500 m or 1,000 m.
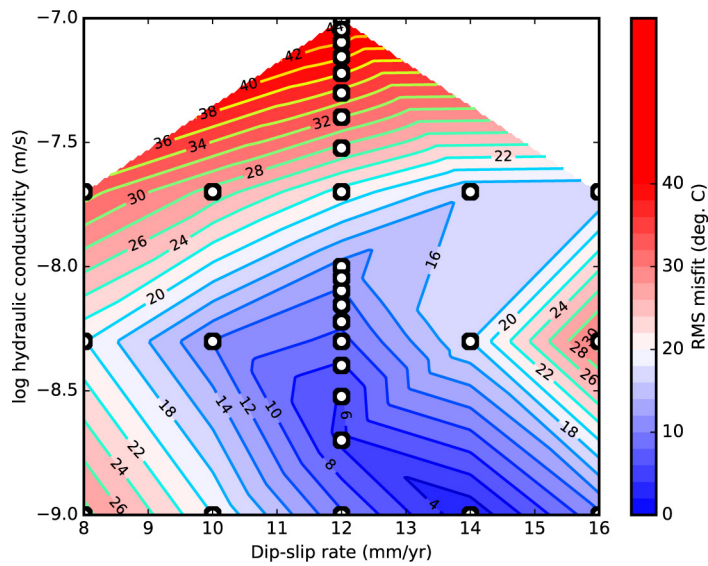
Extended Data Figure 5 | Fit of FEFLOW models to observations at DFDP-2B by varying parameters. Variable parameters are the (uniform) hanging-wall permeability to 3 km below sea level, and the dip-slip rate on the Alpine Fault. White dots indicate the parameter combinations of specific models. RMS, root mean square.
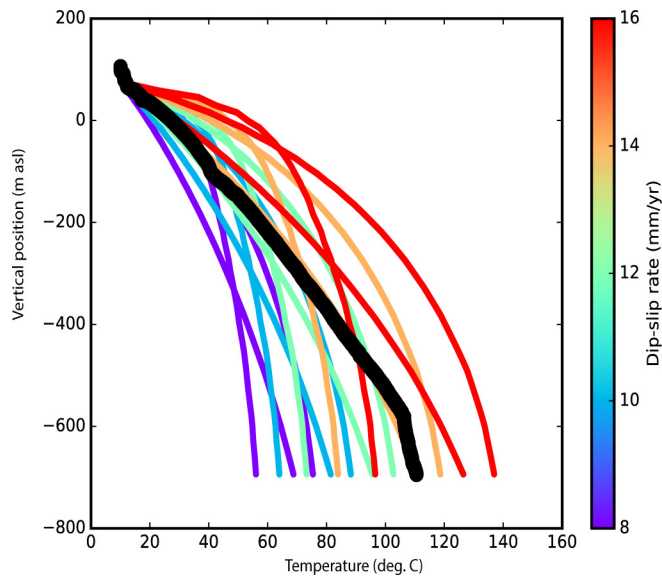
Extended Data Figure 6 | Temperature profiles predicted by models (colour) compared to observations at DFDP-2B (black). (m asl, metres above sea level.)
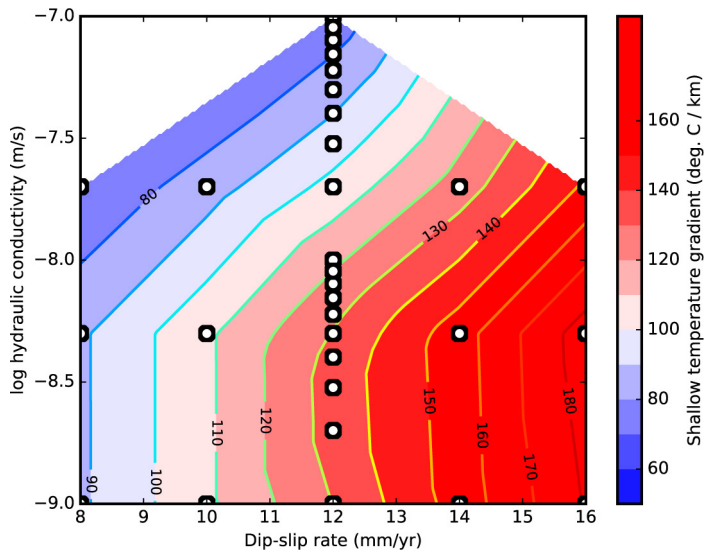
Extended Data Figure 7 | Shallow temperature gradient predicted by models at DFDP-1B. Note that the temperature gradient may be slightly over-estimated by the model, because local fault curvature is not accurately resolved by our model and the DFDP-1B location is placed slightly farther into the base of the hanging wall in the model than it is in reality.

Extended Data Table 1 | Pore fluid pressure head, *H*, determined from borehole length, *L*, equilibrium mud level, *M*, and mud density, *D*

L m	M m	S_M m	D kg m^{-3}	S_{D+} kg m^{-3}	S_{D-} kg m^{-3}	H_i m	S_{Hi+} m	S_{Hi-} m
274.87	-2.8	3.1	1020	5	5	2.7	3.4	3.4
286.87	-3.4	3.1	1071	5	5	16.6	3.6	3.6
396.14	-5.0	3.1	1068	21	23	21.6	8.9	9.7
	-8.4					18.0		
	-7.8					18.6		
	-5.7					20.9		
	-4.1					22.5		
	-3.4					23.4		
	1.2					28.2		
	-2.6					24.2		
	-1.0					25.9		
	-0.6					26.3		
	-0.9					25.9		
396.14	-0.7	0.4	1055	40	40	21.0	15.9	15.9
	0.0					21.7		
	-0.1					21.7		
396.14	-2.5	2.0	1062	8	12	21.8	3.9	5.1
	-5.3					18.8		
486.06	-3.0	3.3	1075	5	5	33.2	4.3	4.3
	-6.6					29.4		
	-9.5					26.2		
520.03	-10.2	3.1	1068	5	5	24.2	4.2	4.2
539.51	-7.3	6.1	1058	5	5	23.2	4.2	4.2
770.29	-18.6	5.5	1091	5	5	49.7	7.1	7.1
	-10.3					58.7		
	-20.6					47.5		
818.00	-16.3	3.1	1098	5	5	61.9	5.3	5.3

$S_L = 0.05$ m.

Estimated standard errors are labelled using the symbol S. Mud levels and hydraulic heads are relative to the local ground surface.

Extended Data Table 2 | Mean pore fluid pressure heads, *H,* and standard errors, *S_H*, determined for each borehole length, *L,* and true vertical depth, *TVD*

L m	TVD m	H m	S_H m
274.87	274.74	2.7	3.4
286.87	286.74	16.6	3.6
396.14	395.30	22.5	0.7
486.06	482.30	29.6	2.0
520.03	514.46	24.2	4.2
539.51	532.57	23.2	4.2
770.29	726.38	52.0	3.4
818.00	762.77	61.9	5.3

See data in Extended Data Table 1. Hydraulic heads are relative to the local ground surface.